

Degradation Chemistry and Kinetic Stabilization of Magnetic CrI<sub>3</sub>

Taiming Zhang, Magdalena Grzeszczyk,\* Jing Li, Wei Yu, Haomin Xu, Peng He, Liming Yang, Zhizhan Qiu, Huihui Lin, Huimin Yang, Jian Zeng, Tao Sun, Zejun Li, Jishan Wu, Ming Lin, Kian Ping Loh, Chenliang Su, Kostya S. Novoselov, Alexandra Carvalho,\* Maciej Koperski,\* and Jiong Lu\*



Cite This: *J. Am. Chem. Soc.* 2022, 144, 5295–5303



Read Online

ACCESS |



Metrics & More

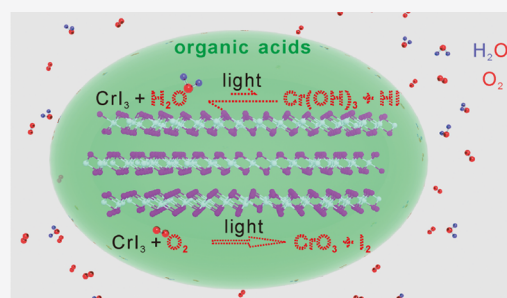


Article Recommendations



Supporting Information

**ABSTRACT:** The discovery of the intrinsic magnetic order in single-layer chromium trihalides (CrX<sub>3</sub>, X = I, Br, and Cl) has drawn intensive interest due to their potential application in spintronic devices. However, the notorious environmental instability of this class of materials under ambient conditions renders their device fabrication and practical application extremely challenging. Here, we performed a systematic investigation of the degradation chemistry of chromium iodide (CrI<sub>3</sub>), the most studied among CrX<sub>3</sub> families, *via* a joint spectroscopic and microscopic analysis of the structural and composition evolution of bulk and exfoliated nanoflakes in different environments. Unlike other air-sensitive 2D materials, CrI<sub>3</sub> undergoes a pseudo-first-order hydrolysis in the presence of pure water toward the formation of amorphous Cr(OH)<sub>3</sub> and hydrogen iodide (HI) with a rate constant of  $k_1 = 0.63 \text{ day}^{-1}$  without light. In contrast, a faster pseudo-first-order surface oxidation of CrI<sub>3</sub> occurs in a pure O<sub>2</sub> environment, generating CrO<sub>3</sub> and I<sub>2</sub> with a large rate constant of  $k_{\text{Cr}} = 4.2 \text{ day}^{-1}$ . Both hydrolysis and surface oxidation of CrI<sub>3</sub> can be accelerated *via* light irradiation, resulting in its ultrafast degradation in air. The new chemical insights obtained allow for the design of an effective stabilization strategy for CrI<sub>3</sub> with preserved optical and magnetic properties. The use of organic acid solvents (*e.g.*, formic acid) as reversible capping agents ensures that CrI<sub>3</sub> nanoflakes remain stable beyond 1 month due to the effective suppression of both hydrolysis and oxidation of CrI<sub>3</sub>.



## INTRODUCTION

The emergent two-dimensional (2D) van der Waals (vdW) magnets not only offer an exciting platform for exploring novel spin physics in a 2D limit<sup>1–5</sup> but also show great promise for spintronic applications.<sup>6–8</sup> The ability to integrate them into layered heterostructures *via* vdW technology further opens up unprecedented opportunities to engineer artificial magnetic quantum materials with tailored properties for quantum technologies.<sup>9</sup>

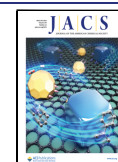
Among the recently emerged vdW magnetic materials,<sup>1,2</sup> CrI<sub>3</sub> has been one of the most widely studied magnetic insulators in the atomically thin limit owing to its long-range ferromagnetic order and tunable interlayer magnetic coupling.<sup>8,10</sup> Monolayer CrI<sub>3</sub> has an out-of-plane magnetic easy axis with a Curie temperature ( $T_C$ ) of 45 K,<sup>11</sup> while few-layer CrI<sub>3</sub> favors interlayer antiferromagnetic coupling, with a  $T_C$  close to that of the bulk (61 K).<sup>1</sup> Such a layer-dependent magnetic ordering can be further tuned by an external electric field, crucial for future on-chip device integration.<sup>3,12</sup>

However, the rapid degradation of CrI<sub>3</sub> thin flakes under ambient conditions represents a major obstacle in both fundamental research and future practical applications.<sup>1,13</sup> The degradation rate of atomically thin CrI<sub>3</sub> flakes in air is much faster (within minutes) than that of other air-sensitive

2D materials [*e.g.*, black phosphorus (BP),<sup>14–17</sup> NbSe<sub>2</sub>,<sup>18</sup> InSe,<sup>19–22</sup> CrGeTe<sub>3</sub>,<sup>2</sup> *etc.*].<sup>23–27</sup> A deep understanding of the degradation chemistry of CrI<sub>3</sub> is crucial for the development of an efficient stabilization strategy.<sup>28–34</sup> Despite extensive efforts devoted toward this goal, insights into the degradation chemistry still remain elusive.<sup>13,35–37</sup> The current CrI<sub>3</sub> stabilization strategies mainly rely on the implementation of a multistep physical encapsulation method including protection *via* a polymer, a hexagonal boron nitride (hBN) layer, and atomic layer deposition of metallic oxide (*e.g.*, Al<sub>2</sub>O<sub>3</sub>).<sup>13,17–22,27,37</sup> Physical encapsulation may offer the advantage of direct device integration but lacks high scalability, solution processability, and the possibility of additional chemical functionalization, which can be achieved by using a chemical stabilization method. The latter strategy has already been exploited to stabilize air-sensitive 2D materials.<sup>34,40–45</sup>

Received: August 23, 2021

Published: March 16, 2022



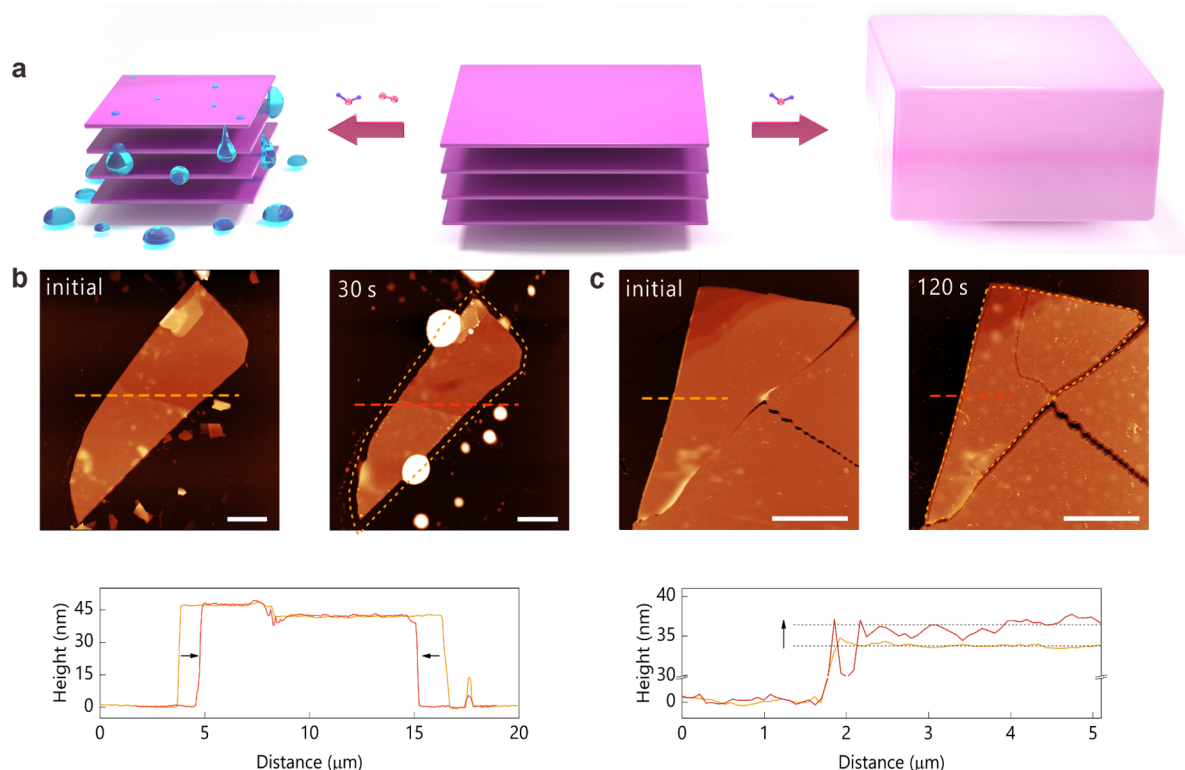


**Figure 1.** Degradation behaviors of  $\text{CrI}_3$  nanoflakes in air and  $\text{H}_2\text{O}$ . (a) Schematic illustration of the degradation behaviors of  $\text{CrI}_3$  in air and in  $\text{H}_2\text{O}$ , and corresponding AFM images and height profiles of the same  $\text{CrI}_3$  nanoflake before and after exposure in air for 30 s (b) and before and after immersion in degassed water for 120 s (c). Note: The orange and red curves in the figure below correspond to the height changes across the dotted lines in the upper left and upper right AFM images, respectively. Scale bar: 5  $\mu\text{m}$ .

Therefore, the development of flexible chemical stabilization methods for 2D magnets is highly valuable.<sup>38–40</sup>

Here, we present a comprehensive study to explain the degradation chemistry of atomically thin  $\text{CrI}_3$  nanoflakes under different conditions. The new insights obtained inspire us to devise an efficient route for the stabilization of this material. Our studies reveal that  $\text{CrI}_3$  undergoes a photo-accelerated and pseudo-first-order hydrolysis reaction in the presence of pure water toward the formation of amorphous  $\text{Cr}(\text{OH})_3$  and  $\text{HI}$  with a rate constant of  $0.71 \text{ day}^{-1}$  ( $0.63 \text{ day}^{-1}$ ) with (without) light irradiation. Similarly, the photo-accelerated and pseudo-first-order oxidation reaction of  $\text{CrI}_3$  readily proceeds in an  $\text{O}_2$  environment to generate  $\text{CrO}_3$  and  $\text{I}_2$  with a larger rate constant of  $4.2 \text{ day}^{-1}$  without light irradiation. The hydrolysis and oxidation reactions result in the ultrafast degradation of  $\text{CrI}_3$  under an ambient environment. The new insights obtained here guided us to devise a new strategy to stabilize  $\text{CrI}_3$  nanoflakes by using organic acids as protection solvents. It is found that  $\text{CrI}_3$  nanoflakes remain stable beyond 1 month in formic acid due to the suppression of hydrolysis and surface oxidation. Our work not only provides a new understanding of the degradation chemistry of  $\text{CrI}_3$  but also demonstrates an efficient chemical stabilization route for  $\text{CrI}_3$ , which can also be useful for the protection of a wide range of reactive 2D magnetic materials.

## RESULTS AND DISCUSSION

We first prepared atomically thin  $\text{CrI}_3$  flakes *via* the mechanical exfoliation of bulk crystals (Figure S1) in a glovebox filled with argon ( $\text{Ar}$ ) gas. Upon exposure to air, rapid degradation of  $\text{CrI}_3$  nanoflakes occurs, as evidenced in the appearance of

bump features within several seconds (Figures 1a,b and S2a), consistent with previous reports.<sup>13</sup> The bumps tend to develop on the edge of the nanoflake and gradually grow in size toward the flake center (Figures 1b and S2a). We also noted that dense, smaller bumps develop on the basal plane, though their size expansion is not as rapid as that of those initiated from the edge, indicating a higher chemical activity on the edge of nanoflakes. After a few minutes, only large droplets remain in place of the original nanoflakes (Figure S2a), indicating complete degradation. In addition, similar to  $\text{BP}$ <sup>33</sup> and  $\text{InSe}$ ,<sup>46</sup> degradation of  $\text{CrI}_3$  slows down significantly with the decrease of the light intensity (Figure S3).

The rapid degradation of  $\text{CrI}_3$  in air may arise from complex chemical reactions involving  $\text{H}_2\text{O}$ ,  $\text{O}_2$ , and light. To explain the role of individual factors, we first designed the experiment to create a single-composition environment for the mechanistic study of the degradation of  $\text{CrI}_3$ . We began with the investigation of the degradation chemistry of  $\text{CrI}_3$  that involves either  $\text{H}_2\text{O}$  or  $\text{O}_2$  with or without light irradiation.

**Degradation Chemistry of  $\text{CrI}_3$  in  $\text{H}_2\text{O}$ .** First, we investigated the possible reaction between  $\text{CrI}_3$  and pure  $\text{H}_2\text{O}$ . Note that a pure  $\text{H}_2\text{O}$  environment is created through  $\text{Ar}$  blowing to eliminate the dissolved gas molecules (e.g.,  $\text{O}_2$ ). Atomic force microscopy (AFM) was employed to monitor the change of  $\text{CrI}_3$  nanoflakes immersed in degassed  $\text{H}_2\text{O}$  (Figure 1a,c). Distinct from the degradation behavior in air, the thickness of the whole nanoflake increases by  $\sim 4 \text{ nm}$  (from  $\sim 33$  to  $\sim 37 \text{ nm}$ ) after its immersion in water for 120 s. This suggests the formation of insoluble products in the reaction between  $\text{CrI}_3$  and  $\text{H}_2\text{O}$ , leading to an increase of the film thickness (Figure S4).

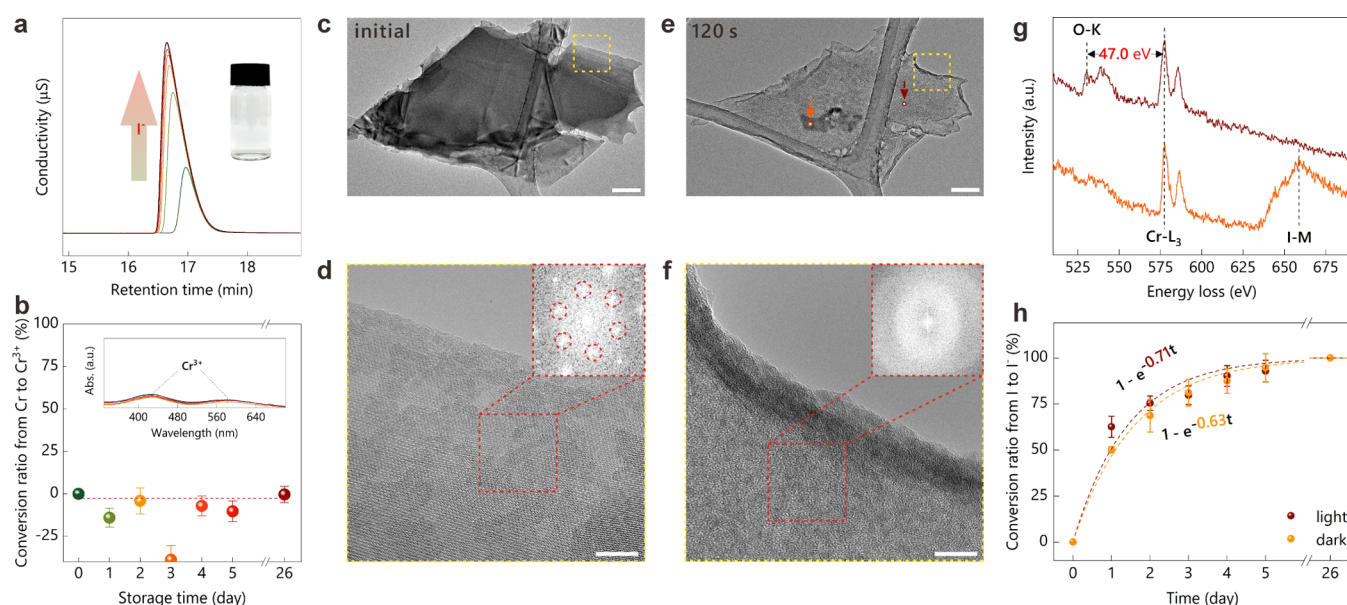
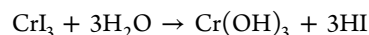


**Figure 2.** Probing the degradation chemistry of  $\text{CrI}_3$  in  $\text{H}_2\text{O}$ . (a) AEC of aqueous solution as a function of time. Inset shows the supernatant solution of the sample at 5 days for AEC. (b) Relative concentration ratio between elemental Cr in  $\text{CrI}_3$  and the  $\text{Cr}^{3+}$  ion after soaking bulk  $\text{CrI}_3$  flakes in  $\text{H}_2\text{O}$  as a function of time, with the corresponding UV–vis spectra obtained from the aqueous solution (inset). Error bars are derived from the standard variation in UV–vis measurements of three sets of parallel experiments. TEM image (c), high-resolution TEM image (d), and corresponding FFT pattern [inset in (d)] of a fresh  $\text{CrI}_3$  nanoflake. TEM image (e), high-resolution TEM image (f), and corresponding FFT pattern [inset in (f)] of the same  $\text{CrI}_3$  nanoflake after a 2 minute reaction in degassed water. (g) EELS spectra were acquired at different surface regions of the  $\text{CrI}_3$  nanoflake after soaking in  $\text{H}_2\text{O}$  for 2 min [marked in (e)]. (h) Plot of the conversion ratio of the iodine anion as a function of time (in days) under different storage conditions (light or dark, Ar). The dotted lines are the corresponding data fitting curves, and the fitting equation was labeled. Error bars are derived from the standard variation from three sets of AEC measurements of parallel samples. Scale bar: 100 nm in (c,e) and 10 nm in (d,f).

To further reveal how  $\text{CrI}_3$  reacts with  $\text{H}_2\text{O}$ , anion exchange chromatography (AEC) and UV–vis spectroscopy were used to track the variation of the anion and cation in water, respectively,<sup>47</sup> while Fourier transform infrared spectroscopy (FT-IR), transmission electron microscopy (TEM), and electron energy loss spectroscopy (EELS) were employed to analyze the component of insoluble products (Figure S5). AEC results reveal a prominent peak at a retention time of  $\sim 17.0$  min attributed to  $\text{I}^-$  (Figures 2a and S6), in contrast to the rather featureless spectra obtained from blank water (Figure S6a). The peak intensity increases as a function of storage time, indicating the generation of  $\text{I}^-$  from the reaction of  $\text{CrI}_3$  with  $\text{H}_2\text{O}$ . In addition, UV–vis spectroscopy reveals a negligible change of the adsorption feature associated with chromium cations ( $\text{Cr}^{3+}$ ), suggesting that no additional chromium cation was generated by the sample degradation (Figures 2b and S7). Therefore, a combination of AEC and UV–vis spectroscopic studies reveals that  $\text{CrI}_3$  undergoes hydrolysis in  $\text{H}_2\text{O}$ , which mainly yields  $\text{I}^-$  anions. This is also further supported by a gradual decrease of the pH value of the solution from  $\sim 6$  to  $\sim 4$ , attributed to the formation of HI from the hydrolysis of  $\text{CrI}_3$ .

In addition to the analysis of the soluble components, the insoluble products of the reaction with  $\text{H}_2\text{O}$  were also identified. XPS and FT-IR spectra acquired indicate that an insoluble product is likely to be chromic hydroxide (Figures S8, S9), as evidenced by the observation of the features of  $\text{Cr}(\text{OH})_3$  in Cr 2p and O 1s spectra, a bending mode of Cr–O at  $\sim 545\text{ cm}^{-1}$  and a bending mode of O–H at  $\sim 1619\text{ cm}^{-1}$  in the FT-IR spectra.<sup>48–50</sup> In addition, we also employed TEM and EELS (Figure 2c–g) to further probe the crystallinity and composition of the materials before and after the reaction with

$\text{H}_2\text{O}$ . Prior to the reaction with  $\text{H}_2\text{O}$ , a fresh  $\text{CrI}_3$  nanoflake with a lateral dimension of  $\sim 800\text{ nm}$  (Figure 2c) shows a high crystalline state with a hexagonal lattice (Figure 2d) and a characteristic diffraction pattern, as revealed in the corresponding fast Fourier transform (FFT) analysis varied the monocrystalline  $\text{CrI}_3$  ( $C2/m$ ). After 2 min of soaking in  $\text{H}_2\text{O}$  (Figure 2e), an obvious change of the TEM contrast was observed in a large portion of the  $\text{CrI}_3$  nanoflake, which indicates a significant degradation. Note that only a small area of the  $\text{CrI}_3$  nanoflake survived. The disappearance of the  $\text{CrI}_3$  lattice in degraded regions, in combination with the resulting indistinct FFT pattern (Figure 2f), reflects a crystalline-to-amorphous transition as the reaction proceeds. In a subsequent EELS analysis, it was noted that the differences between the Cr L-edge features of the EELS spectra acquired in the degraded sample regions (deep red curve in Figure 2g) and in the surviving sample regions (orange curve in Figure 2g) were negligible. However, a new feature located at  $530.5\text{ eV}$  is observed in the degraded region and is attributed to the O K-edge, which suggests that the insoluble product derived from hydrolysis is likely to be amorphous chromium (III) hydroxide.<sup>51</sup> Based on these spectroscopic studies and on TEM imaging, the degradation reaction between  $\text{CrI}_3$  and  $\text{H}_2\text{O}$  can be described using the following chemical equation



The degradation kinetics of bulk  $\text{CrI}_3$  flakes in  $\text{H}_2\text{O}$  was further studied by tracking the time-dependent quantitative variation of the  $\text{I}^-$  concentration with and without light irradiation. Figure 2h reveals a monoexponential increase of the relative conversion ratio of elemental I in  $\text{CrI}_3$  into  $\text{I}^-$  as a function of time, suggesting a pseudo-first-order reaction



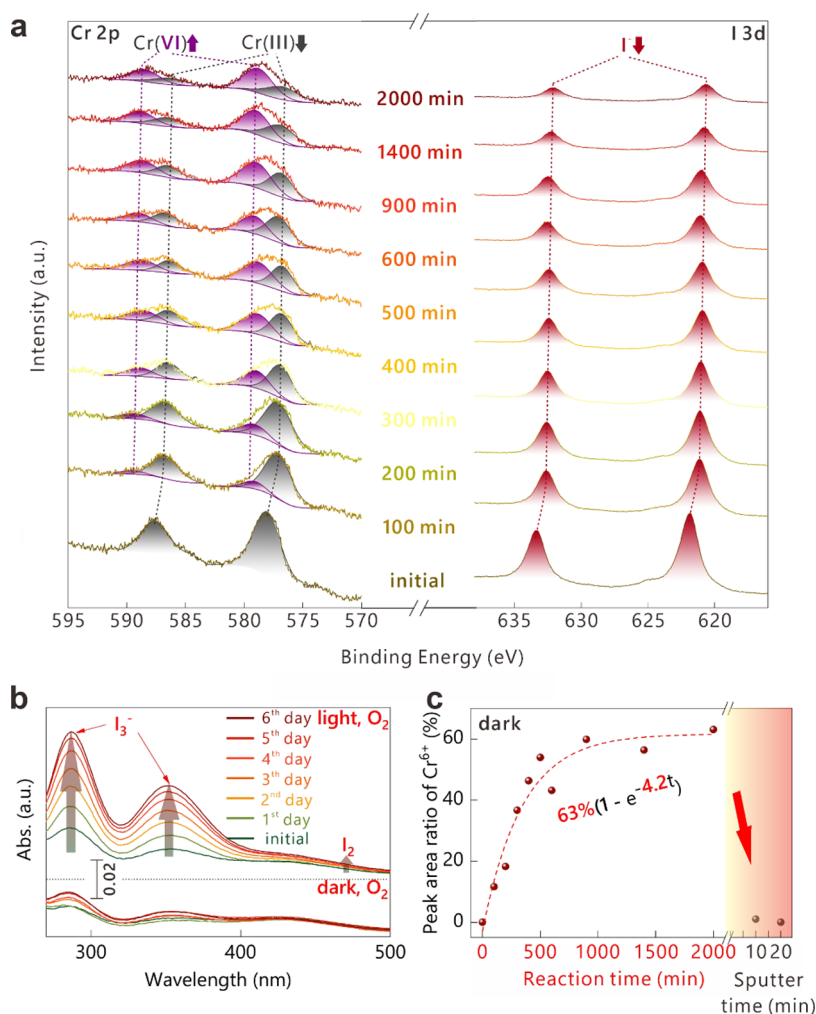


**Figure 3.** Probing the degradation chemistry of CrI<sub>3</sub> in O<sub>2</sub>. (a) *In situ* XPS Cr 2p and I 3d spectra of bulk CrI<sub>3</sub> in a pure oxygen atmosphere within 2000 min of the start of the degradation. (b) UV-vis spectra of aqueous solutions containing bulk CrI<sub>3</sub> and dissolved oxygen under light (up) and dark (down) as a function of time. (c) Increase and decrease of the peak area ratio of hexavalent chromium [ $A_{\text{Cr(VI)}}/(A_{\text{Cr(VI)}} + A_{\text{Cr(III)}})$ ] with time. The dashed line is the corresponding data fitting curve for oxidation within 2000 min, and the fitting equation is labeled. The oxidized surface can be removed *via* Ar sputtering (orange region).

between CrI<sub>3</sub> and H<sub>2</sub>O.<sup>47</sup> Here, the concentration of H<sub>2</sub>O and Cr(OH)<sub>3</sub> (low  $K_{\text{sp}}$ :  $6.3 \times 10^{-31}$ ) can be assumed to be constant. Therefore, the hydrolysis rate of CrI<sub>3</sub>,  $r$ , can be written as

$$r = -\frac{d[\text{CrI}_3]}{dt} = \frac{d[\text{I}^-]}{3 dt}$$

The concentrations of produced I<sup>-</sup> ([I<sup>-</sup>]) as a function of reaction time ( $t$ ), can be deduced from the equation

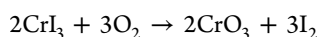
$$[\text{I}^-] = 3[\text{CrI}_3]_0(1 - e^{-k_1 t})$$

where  $[\text{CrI}_3]_0$  is the concentration of CrI<sub>3</sub> at  $t = 0$  and  $k_1$  is the rate constant of the generation of I<sup>-</sup>. Monoexponential fitting yields reaction rate constants ( $k_1$ ) of 0.71 and 0.63 day<sup>-1</sup> with and without light, respectively. This also points out that light irradiation accelerates the hydrolysis.

#### Degradation Chemistry of CrI<sub>3</sub> in an O<sub>2</sub> Environment.

Next, we probe the reaction between CrI<sub>3</sub> and O<sub>2</sub> using *in situ* X-ray photoelectron spectroscopy (XPS). Both the bulk and nanoflakes may undergo similar surface oxidation. However, bulk CrI<sub>3</sub> samples can be readily cleaved under ultra-high vacuum conditions to obtain fresh surfaces for *in situ* XPS. We

collected a series of XPS spectra to track the composition change of the bulk CrI<sub>3</sub> flake stored in a pure O<sub>2</sub> atmosphere at close to atmospheric pressure (Figure 3a). The features at 578.1 and 587.6 eV associated with Cr 2p become gradually broadened, while peaks centered at 621.8 and 633.3 eV attributed to I 3d are gradually weakened as a function of time (the area of the peak centered at 621.8 eV drops by ~72% after 2000 min). In addition, a new set of peaks appear at 579.1 and 589.3 eV, higher than that of Cr 2p of intrinsic CrI<sub>3</sub>. These new peaks can be assigned to Cr(VI),<sup>52</sup> indicating the oxidation of CrI<sub>3</sub> in a pure O<sub>2</sub> environment. A decrease in the peak intensity related to I 3d indicates the desorption of the I element. A gradual red shift in peak position as a function of time is likely due to an increased surface charging effect as the oxidation proceeds. In addition, we also observed that elemental iodine (I<sub>2</sub>) can be generated in water containing dissolved O<sub>2</sub> and CrI<sub>3</sub> (Figure 3b), indicating that CrI<sub>3</sub> reacts with O<sub>2</sub> to form I<sub>2</sub>. Moreover, the formation rate of I<sub>2</sub> from oxidation can be further accelerated by exposure to light (Figure 3b). All these observations suggest that the reaction of CrI<sub>3</sub> with O<sub>2</sub> leads to the formation of I<sub>2</sub> and CrO<sub>3</sub>, which can be described by the following equation



Similar to the hydrolysis reaction between  $\text{CrI}_3$  and  $\text{H}_2\text{O}$ , the kinetics study for the reaction with  $\text{O}_2$  also reveals a monoexponential increase in the peak area ratio of  $\text{Cr(VI)}$  as a function of time (Figure 3c), suggesting a pseudo-first-order reaction. The corresponding rate constant  $k_{\text{Cr}}$  for the reaction in dark under a pure  $\text{O}_2$  atmosphere ( $\sim 2$  bar) was determined to be  $4.2 \text{ day}^{-1}$ , through a monoexponential fitting of the experimental data. Such a value is nearly an order of magnitude higher than that of the hydrolysis reaction, suggesting a much faster oxidation reaction.

In addition, the oxidation ceases at a later stage [a maximum of  $\sim 63 \text{ mol } \%$  Cr was oxidized into  $\text{Cr(VI)}$ ], as shown in Figure 3c, suggesting a self-limiting oxidation process. That is to say, the surface of  $\text{CrI}_3$  was oxidized into  $\text{Cr(VI)}$ , and the remaining  $\text{CrI}_3$  layers buried underneath can survive due to the protection from the surface oxide layer. This is also taking into account the surface sensitivity of the XPS technique, which only acquires photoemission electrons within a depth of several nanometers from the top surface. Moreover, the peak area ratio of  $\text{Cr(VI)}$  drops to nearly zero after Ar sputtering (orange region in Figure 3c) on the surface of bulk  $\text{CrI}_3$ .

We have used density functional theory (DFT) calculations<sup>53</sup> to confirm the feasibility of these reactions. The binding energy for a physisorbed oxygen molecule is  $0.18 \text{ eV}$ . The calculated energetic profile (Figures 4a, S10, and Table S1) reveals that the subsequent reaction between  $\text{O}_2$  and  $\text{CrI}_3$  requires overcoming a moderate energy barrier of  $1.6 \text{ eV}$ , which is anticipated to be further lowered due to the presence of atomic defects in the materials (Figure S11). Nevertheless, the whole reaction is energetically favorable with an energy

gain of  $0.89 \text{ eV}$ . The reaction between  $\text{O}_2$  and  $\text{CrI}_3$  results in the oxidation of  $\text{CrI}_3$  (O atoms are chemically bonded to Cr atoms, Figure 4b,c) and a release of  $\text{I}_2$ , consistent with the experimental observation. We have not performed similar calculations for the reaction between  $\text{CrI}_3$  and liquid water due to the difficulty in representing the liquid behavior and energetics, which are different from those of gaseous water. In case of gaseous  $\text{H}_2\text{O}$ , our DFT calculation reveals that hydrolysis of  $\text{CrI}_3$  occurs through the dissociation of  $\text{H}_2\text{O}$  molecules and release of  $\text{HI}$ , wherein hydrogen and hydroxyl bind to adjacent iodine atoms and chromium atoms, respectively. In addition,  $\text{H}_2\text{O}$  also reacts with iodine vacancies, which is an endothermic process. As the reaction with water proceeds,  $\text{CrI}_3$  can be fully converted into  $\text{Cr(OH)}_3$  (Figure S12 and Table S1).

With the help of calculations, we draw a picture of possible degradation processes, and as summarized in Figure S13, the hydrolysis and oxidation of  $\text{CrI}_3$  are major chemical reactions attributed to its rapid degradation in air (Figure S14, 15), while the light is found to accelerate the whole degradation process likely due to the spin transition triggered in the case of the oxidation reaction (Figure S10) and effects of heat from illumination. New chemical insights obtained here help us develop an efficient strategy for the stabilization of  $\text{CrI}_3$  via a judicious choice of acidic solvents, which can suppress both hydrolysis and oxidation.

**Stabilization of  $\text{CrI}_3$  in Organic Acid Solvents.** A trace amount of water and oxygen in the environment, which are hard to remove completely, will induce the degradation of  $\text{CrI}_3$ . Typically, the concentration of dissolved oxygen is reduced in solvents, which thus suppresses the oxidation.<sup>41,54</sup> Moreover, an increase of the proton concentration is expected to inhibit the hydrolysis reaction of  $\text{CrI}_3$  (Figure 5a), but this has to eliminate the aqueous acidic solution due to the presence of a large amount of  $\text{H}_2\text{O}$ . Even in a strong acidic aqueous solution ( $\text{pH} \sim 2$ ), bulk  $\text{CrI}_3$  flakes are completely degraded within 3 days (Figure S16). Therefore, our key protection idea lies in the choice of the organic acid solution (e.g., formic acid, the simplest organic acid) to suppress the chemical reactions discussed above.

First, the effective protection of  $\text{CrI}_3$  in formic acid can be verified based on the negligible color variation of the solvents containing bulk  $\text{CrI}_3$  in an ambient environment, in contrast to a fast color change for  $\text{CrI}_3$  flakes stored in other nonacidic solvents, such as acetone, hexane, acetonitrile, and so forth (Figures 5b and S17). The morphology of the  $\text{CrI}_3$  nanoflake still remains intact after being kept in formic acid for 2 weeks (Figure 5c,d). Energy-dispersive X-ray spectroscopy (EDS) mapping of Cr and I elements (Figure 5e,f) combined with the observation of the characteristic  $E_g$  mode at  $107 \text{ cm}^{-1}$  and  $A_{1g}$  mode at  $129 \text{ cm}^{-1}$  in the Raman spectrum (Figure 5g–i) further verifies that the crystal structure of  $\text{CrI}_3$  is preserved<sup>13,55,56</sup> during storage in formic acid for 14 days. In addition, a similar protection effect was obtained for  $\text{CrI}_3$  kept in acetic acid (Figure S18), while  $\text{CrI}_3$  undergoes an obvious degradation in other commonly used organic solvents within the same time frame (Figure S19). It is noted that  $\text{CrI}_3$  nanoflakes stored in formic acid for 1.5 months present negligible changes, but the nanoflakes stored in acetic acid show partial degradation (Figure S20).

To reveal the microscopic picture of formic acid stabilization, DFT calculations were used (Figure S22). It is concluded that formic acid molecules ( $\text{HCOOH}$ ) tend to

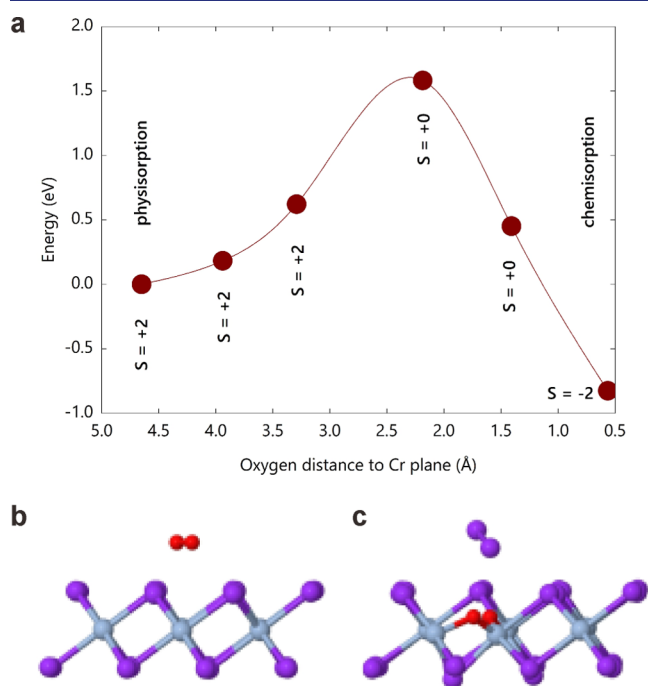


**Figure 4.** DFT calculations of oxygen adsorption with release of  $\text{I}_2$ . (a) Energy profile for the reaction between physisorbed  $\text{O}_2$  and  $\text{CrI}_3$ , resulting in a chemisorbed oxygen dimer and with release of  $\text{I}_2$ , along with the respective structures for the physisorbed state (b) and chemisorbed state (c). S indicates the spin state of the structure relative to the original spin state of  $\text{CrI}_3$ , in units of the electron spin.

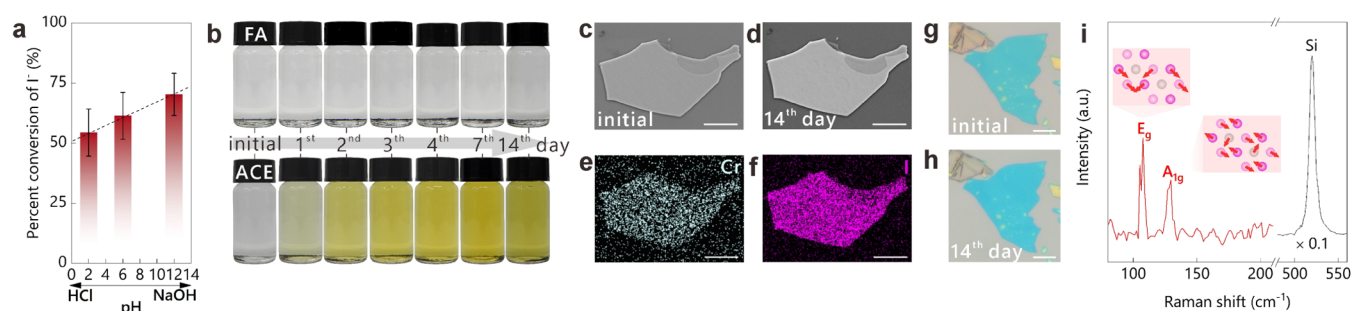


**Figure 5.** Stabilizing  $\text{CrI}_3$  in organic acid. (a) Percentage of the conversion of  $\text{CrI}_3$  into  $\text{I}^-$  for bulk  $\text{CrI}_3$  flakes immersed in water with different pH values after the degradation reaction ceases (no degassing). The percentage of conversion decreases with the decrease of pH, indicating that the acid inhibits the hydrolysis of  $\text{CrI}_3$ . (b) Optical photographs of bulk  $\text{CrI}_3$  flakes stored in different organic solvents under an ambient environment. FA: formic acid and ACE: acetone. SEM images of the same  $\text{CrI}_3$  nanoflake soaking in FA at the initial state (c) and after 14 days (d) and EDS mapping of the Cr and I elements (e,f) of the flake after 14 days. Optical microscopy images of the same  $\text{CrI}_3$  nanoflake soaking in FA under ambient conditions at the initial state (g) and after 14 days (h). (i) Raman spectra of the  $\text{CrI}_3$  nanoflake in (g):  $E_g$  mode (up) and  $A_{1g}$  mode (down). Note: The silicon reference signal was reduced by a factor of 10. Scale bar: 10  $\mu\text{m}$ .

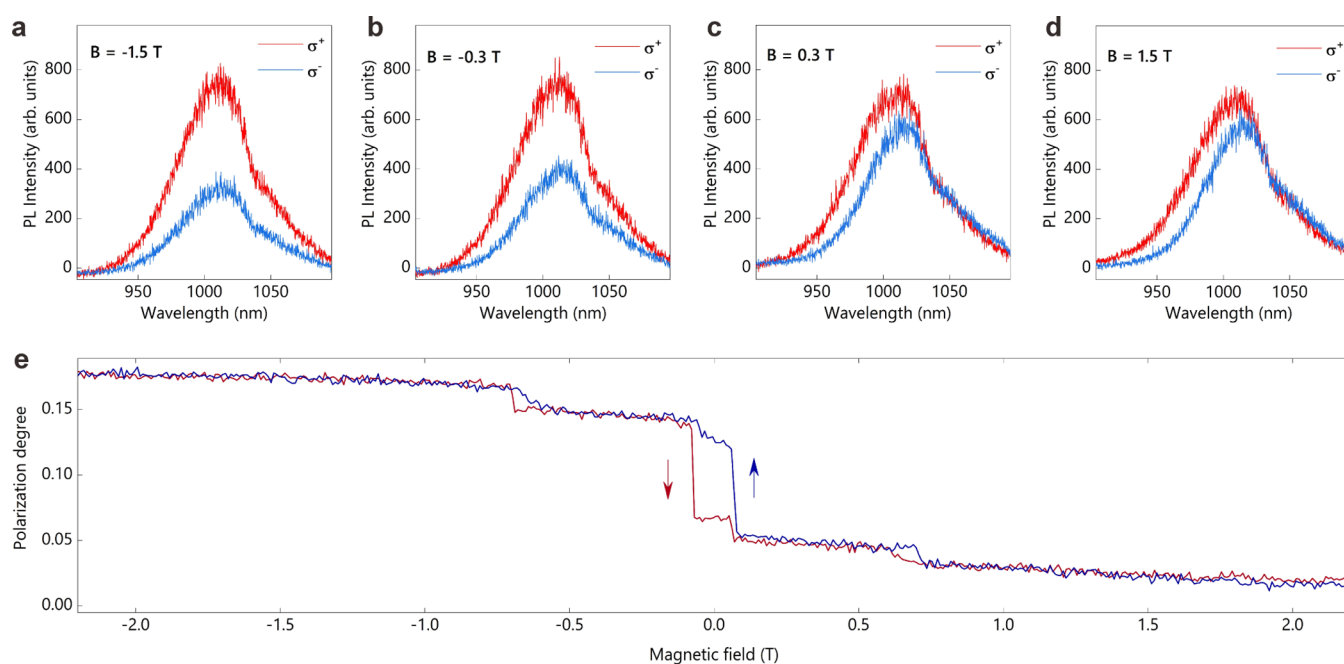


**Figure 6.** (a–d) The low-temperature (1.6 K) PL spectra under microscopic 532 nm excitation of an exfoliated  $\text{CrI}_3$  nanoflake, which was soaked in formic acid, demonstrate a broad near-infrared emission band akin to the optical response of the hBN-encapsulated  $\text{CrI}_3$  layers. The emission observed below the Curie temperature is characterized by a finite circular polarization degree. (e) Its evolution in a magnetic field displays a hysteresis indicative of the ferromagnetic order of the magnetic moments associated with the Cr atoms.

physically adsorb on perfect  $\text{CrI}_3$  but tend not to react destructively with it and that  $\text{COOH}$  radicals can bind to iodine vacancies. In this case, the vacancies and basal plane are passivated and will not serve as binding sites for water and oxygen dissociation, and protons are generated with the formation of  $\text{COOH}$  radicals, which further slow the hydrolysis reaction of  $\text{CrI}_3$ .

The preservation of the exfoliated  $\text{CrI}_3$  flakes within organic acids enables probing their electronic and magnetic properties through the inspection of open and unprotected films. In this regard, we have investigated the magneto-photoluminescence (PL) response of  $\text{CrI}_3$  layers deposited on Si/SiO<sub>2</sub> substrates comparatively with those that are protected through hBN encapsulation. As demonstrated in Figure 6, the PL observed in the  $\text{CrI}_3$  nanoflake treated with organic acids is characterized by an emission band in the near-infrared spectral region. Such an optical response is characteristic of Frenkel excitons at the

limit of strong electron–phonon coupling.<sup>57</sup> The intensity of the PL signal resolved by circular polarization and monitored as a function of the magnetic field reveals hysteresis. This observation signifies a coupling between the angular momentum of the photoexcited carriers and the magnetic moments of Cr atoms. In the presence of such a coupling, the population of the excitons is redistributed between spin-split excitonic levels, which are active in polarizations. Hence, monitoring the polarization degree of the PL grants insights into the evolution of magnetization state of  $\text{CrI}_3$ . The dominant contribution to the hysteresis centered around 0 T is indicative of the emergent global ferromagnetism for few-layer  $\text{CrI}_3$ , while the multiple steps observed from  $-1$  T to 1 T can be attributed to partial flipping of antiferromagnetically coupled adjacent layers in combination with the domain-dependent hysteresis response observable in few-layer and bulk chromium trihalide crystals.<sup>58–60</sup> Further examples of hyste-



resis loops seen in unprotected flakes of various thicknesses for  $\text{CrI}_3$  and  $\text{CrBr}_3$  materials are demonstrated in Figures S24 and S25. Qualitatively, we found that immersion in organic acid is a valid alternative for physical protection of the 2D magnets, enabling further progress toward investigations of their fundamental properties and their incorporation into structures of technological importance. Compared with the physical protection methods previously reported,<sup>13,17–22,27,37</sup> this wet chemical stabilization strategy offers the additional advantages of high scalability and processibility, especially under atmospheric conditions, which are of importance for the large-scale and low-cost fabrication of 2D magnet-based devices.

## CONCLUSIONS

In summary, we have gained a new understanding of the degradation chemistry of a prototypical 2D magnetic material,  $\text{CrI}_3$ , in different chemical environments. Our studies uncover that  $\text{CrI}_3$  undergoes a pseudo-first-order hydrolysis in pure water with the formation of  $\text{Cr}(\text{OH})_3$  and  $\text{HI}$ , while a faster pseudo-first-order surface oxidation of this material readily occurs in an  $\text{O}_2$  environment to generate  $\text{CrO}_3$  and  $\text{I}_2$ . Both hydrolysis and surface oxidation of  $\text{CrI}_3$  can be accelerated with light irradiation, attributed to its ultrafast degradation in air. The insights thus obtained allow us to develop an effective protection strategy by exploiting organic acids as reversible capping agents to preserve its optical and magnetic properties.  $\text{CrI}_3$  remains stable in organic acids beyond 1 month due to the suppression of both the hydrolysis and the surface oxidation. Our findings may further boost both fundamental research and the future technological application of air-sensitive magnetic quantum materials.

## ASSOCIATED CONTENT

### Supporting Information

The Supporting Information is available free of charge at <https://pubs.acs.org/doi/10.1021/jacs.1c08906>.

Additional experimental details, materials, methods, and theoretical calculation results of the energetic profile and reaction enthalpies (PDF)

## AUTHOR INFORMATION

### Corresponding Authors

**Magdalena Grzeszczyk** – Department of Materials Science and Engineering, National University of Singapore, Singapore 117575, Singapore; Institute for Functional Intelligent Materials, National University of Singapore, Singapore 117544, Singapore; Email: [msemjg@nus.edu.sg](mailto:msemjg@nus.edu.sg)

**Alexandra Carvalho** – Institute for Functional Intelligent Materials, National University of Singapore, Singapore 117544, Singapore; Centre for Advanced 2D Materials, National University of Singapore, Singapore 117546, Singapore; Email: [carvalho@nus.edu.sg](mailto:carvalho@nus.edu.sg)

**Maciej Koperski** – Department of Materials Science and Engineering, National University of Singapore, Singapore 117575, Singapore; Institute for Functional Intelligent Materials, National University of Singapore, Singapore 117544, Singapore; [orcid.org/0000-0002-8301-914X](https://orcid.org/0000-0002-8301-914X); Email: [msemaci@nus.edu.sg](mailto:msemaci@nus.edu.sg)

**Jiong Lu** – Department of Chemistry, National University of Singapore, Singapore 117543, Singapore; Institute for Functional Intelligent Materials, National University of

Singapore, Singapore 117544, Singapore; [orcid.org/0000-0002-3690-8235](https://orcid.org/0000-0002-3690-8235); Email: [chmluj@nus.edu.sg](mailto:chmluj@nus.edu.sg)

## Authors

**Taiming Zhang** – SZU-NUS Collaborative Innovation Center for Optoelectronic Science & Technology, International Collaborative Laboratory of 2D Materials for Optoelectronic Science and Technology of Ministry of Education, Institute of Microscale Optoelectronics, Shenzhen University, Shenzhen 518060, China; Department of Chemistry, National University of Singapore, Singapore 117543, Singapore; [orcid.org/0000-0002-0623-652X](https://orcid.org/0000-0002-0623-652X)

**Jing Li** – Department of Chemistry, National University of Singapore, Singapore 117543, Singapore; [orcid.org/0000-0002-5627-4153](https://orcid.org/0000-0002-5627-4153)

**Wei Yu** – Department of Chemistry, National University of Singapore, Singapore 117543, Singapore; [orcid.org/0000-0003-3468-3439](https://orcid.org/0000-0003-3468-3439)

**Haomin Xu** – Department of Chemistry, National University of Singapore, Singapore 117543, Singapore

**Peng He** – SZU-NUS Collaborative Innovation Center for Optoelectronic Science & Technology, International Collaborative Laboratory of 2D Materials for Optoelectronic Science and Technology of Ministry of Education, Institute of Microscale Optoelectronics, Shenzhen University, Shenzhen 518060, China; Department of Chemistry, National University of Singapore, Singapore 117543, Singapore

**Liming Yang** – Department of Chemical and Biomolecular Engineering, National University of Singapore, Singapore 117585, Singapore

**Zhizhan Qiu** – Department of Chemistry, National University of Singapore, Singapore 117543, Singapore

**Huihui Lin** – Department of Chemistry, National University of Singapore, Singapore 117543, Singapore

**Huimin Yang** – Department of Chemistry, National University of Singapore, Singapore 117543, Singapore; [orcid.org/0000-0003-4949-0787](https://orcid.org/0000-0003-4949-0787)

**Jian Zeng** – Department of Chemistry, National University of Singapore, Singapore 117543, Singapore

**Tao Sun** – Department of Chemistry, National University of Singapore, Singapore 117543, Singapore

**Zejun Li** – Department of Chemistry, National University of Singapore, Singapore 117543, Singapore; [orcid.org/0000-0002-7582-0674](https://orcid.org/0000-0002-7582-0674)

**Jishan Wu** – Department of Chemistry, National University of Singapore, Singapore 117543, Singapore; [orcid.org/0000-0002-8231-0437](https://orcid.org/0000-0002-8231-0437)

**Ming Lin** – Institute of Materials Research and Engineering, Agency for Science, Technology and Research (A\*STAR), Singapore 138634, Singapore

**Kian Ping Loh** – Department of Chemistry, National University of Singapore, Singapore 117543, Singapore; [orcid.org/0000-0002-1491-743X](https://orcid.org/0000-0002-1491-743X)

**Chenliang Su** – SZU-NUS Collaborative Innovation Center for Optoelectronic Science & Technology, International Collaborative Laboratory of 2D Materials for Optoelectronic Science and Technology of Ministry of Education, Institute of Microscale Optoelectronics, Shenzhen University, Shenzhen 518060, China; [orcid.org/0000-0002-8453-1938](https://orcid.org/0000-0002-8453-1938)

**Kostya S. Novoselov** – Department of Materials Science and Engineering, National University of Singapore, Singapore 117575, Singapore; Institute for Functional Intelligent

Materials, National University of Singapore, Singapore 117544, Singapore

Complete contact information is available at:  
<https://pubs.acs.org/10.1021/jacs.1c08906>

## Notes

The authors declare no competing financial interest.

## ACKNOWLEDGMENTS

J.L. acknowledges support from MOE grants: MOE2019-T2-2-044 and MOE-T2EP50121-0008. T.Z. acknowledges financial support from the Postdoctoral Research Foundation of China (2020M672774).

## REFERENCES

- (1) Huang, B.; Clark, G.; Navarro-Moratalla, E.; Klein, D. R.; Cheng, R.; Seyler, K. L.; Zhong, D.; Schmidgall, E.; McGuire, M. A.; Cobden, D. H.; Yao, W.; Xiao, D.; Jarillo-Herrero, P.; Xu, X. Layer-dependent ferromagnetism in a van der Waals crystal down to the monolayer limit. *Nature* **2017**, *546*, 270.
- (2) Gong, C.; Li, L.; Li, Z.; Ji, H.; Stern, A.; Xia, Y.; Cao, T.; Bao, W.; Wang, C.; Wang, Y.; Qiu, Z. Q.; Cava, R. J.; Louie, S. G.; Xia, J.; Zhang, X. Discovery of intrinsic ferromagnetism in two-dimensional van der Waals crystals. *Nature* **2017**, *546*, 265.
- (3) Jiang, S.; Shan, J.; Mak, K. F. Electric-field switching of two-dimensional van der Waals magnets. *Nat. Mater.* **2018**, *17*, 406–410.
- (4) Sun, Z.; Yi, Y.; Song, T.; Clark, G.; Huang, B.; Shan, Y.; Wu, S.; Huang, D.; Gao, C.; Chen, Z.; McGuire, M.; Cao, T.; Xiao, D.; Liu, W.-T.; Yao, W.; Xu, X.; Wu, S. Giant nonreciprocal second-harmonic generation from antiferromagnetic bilayer CrI<sub>3</sub>. *Nature* **2019**, *572*, 497–501.
- (5) Chen, W.; Sun, Z.; Wang, Z.; Gu, L.; Xu, X.; Wu, S.; Gao, C. Direct observation of van der Waals stacking-dependent interlayer magnetism. *Science* **2019**, *366*, 983–987.
- (6) Song, T.; Cai, X.; Tu, M. W.-Y.; Zhang, X.; Huang, B.; Wilson, N. P.; Seyler, K. L.; Zhu, L.; Taniguchi, T.; Watanabe, K.; McGuire, M. A.; Cobden, D. H.; Xiao, D.; Yao, W.; Xu, X. Giant tunneling magnetoresistance in spin-filter van der Waals heterostructures. *Science* **2018**, *360*, 1214–1218.
- (7) Wang, X.; Tang, J.; Xia, X.; He, C.; Zhang, J.; Liu, Y.; Wan, C.; Fang, C.; Guo, C.; Yang, W.; Guang, Y.; Zhang, X.; Xu, H.; Wei, J.; Liao, M.; Lu, X.; Feng, J.; Li, X.; Peng, Y.; Wei, H.; Yang, R.; Shi, D.; Zhang, X.; Han, Z.; Zhang, Z.; Zhang, G.; Yu, G.; Han, X. Current-driven magnetization switching in a van der Waals ferromagnet Fe<sub>3</sub>GeTe<sub>2</sub>. *Sci. Adv.* **2019**, *5*, No. eaaw8904.
- (8) Huang, B.; McGuire, M. A.; May, A. F.; Xiao, D.; Jarillo-Herrero, P.; Xu, X. Emergent phenomena and proximity effects in two-dimensional magnets and heterostructures. *Nat. Mater.* **2020**, *19*, 1276–1289.
- (9) Gong, C.; Zhang, X. Two-dimensional magnetic crystals and emergent heterostructure devices. *Science* **2019**, *363*, No. eaav4450.
- (10) Qiu, Z.; Holwill, M.; Olsen, T.; Lyu, P.; Li, J.; Fang, H.; Yang, H.; Kashchenko, M.; Novoselov, K. S.; Lu, J. Visualizing atomic structure and magnetism of 2D magnetic insulators via tunneling through graphene. *Nat. Commun.* **2021**, *12*, 70.
- (11) Liu, J.; Sun, Q.; Kawazoe, Y.; Jena, P. Exfoliating biocompatible ferromagnetic Cr-trihalide monolayers. *Phys. Chem. Chem. Phys.* **2016**, *18*, 8777–8784.
- (12) Jiang, S.; Li, L.; Wang, Z.; Mak, K. F.; Shan, J. Controlling magnetism in 2D CrI<sub>3</sub> by electrostatic doping. *Nat. Nanotechnol.* **2018**, *13*, 549–553.
- (13) Shcherbakov, D.; Stepanov, P.; Weber, D.; Wang, Y.; Hu, J.; Zhu, Y.; Watanabe, K.; Taniguchi, T.; Mao, Z.; Windl, W.; Goldberger, J.; Bockrath, M.; Lau, C. N. Raman spectroscopy, photocatalytic degradation, and stabilization of atomically thin chromium tri-iodide. *Nano Lett.* **2018**, *18*, 4214–4219.
- (14) Huang, Y.; Qiao, J.; He, K.; Bliznakov, S.; Sutter, E.; Chen, X.; Luo, D.; Meng, F.; Su, D.; Decker, J.; Ji, W.; Ruoff, R. S.; Sutter, P. Interaction of black phosphorus with oxygen and water. *Chem. Mater.* **2016**, *28*, 8330–8339.
- (15) Hu, Z.; Li, Q.; Lei, B.; Zhou, Q.; Xiang, D.; Lyu, Z.; Hu, F.; Wang, J.; Ren, Y.; Guo, R.; Goki, E.; Wang, L.; Han, C.; Wang, J.; Chen, W. Water-Catalyzed Oxidation of Few-Layer Black Phosphorus in a Dark Environment. *Angew. Chem., Int. Ed.* **2017**, *56*, 9131–9135.
- (16) Liu, X.; Chen, K.; Li, X.; Xu, Q.; Weng, J.; Xu, J. Electron Matters: Recent Advances in Passivation and Applications of Black Phosphorus. *Adv. Mater.* **2021**, *33*, 2005924.
- (17) Wood, J. D.; Wells, S. A.; Jariwala, D.; Chen, K.-S.; Cho, E.; Sangwan, V. K.; Liu, X.; Lauhon, L. J.; Marks, T. J.; Hersam, M. C. Effective Passivation of Exfoliated Black Phosphorus Transistors against Ambient Degradation. *Nano Lett.* **2014**, *14*, 6964–6970.
- (18) Cao, Y.; Mishchenko, A.; Yu, G. L.; Khestanova, E.; Rooney, A. P.; Prestat, E.; Kretinin, A. V.; Blake, P.; Shalom, M. B.; Woods, C.; Chapman, J.; Balakrishnan, G.; Grigorieva, I. V.; Novoselov, K. S.; Piot, B. A.; Potemski, M.; Watanabe, K.; Taniguchi, T.; Haigh, S. J.; Geim, A. K.; Gorbachev, R. V. Quality heterostructures from two-dimensional crystals unstable in air by their assembly in inert atmosphere. *Nano Lett.* **2015**, *15*, 4914–4921.
- (19) Li, M.; Lin, C.-Y.; Yang, S.-H.; Chang, Y.-M.; Chang, J.-K.; Yang, F.-S.; Zhong, C.; Jian, W.-B.; Lien, C.-H.; Ho, C.-H.; Liu, H.-J.; Huang, R.; Li, W.; Lin, Y.-F.; Chu, J. High Mobilities in Layered InSe Transistors with Indium-Encapsulation-Induced Surface Charge Doping. *Adv. Mater.* **2018**, *30*, 1803690.
- (20) Wells, S. A.; Henning, A.; Gish, J. T.; Sangwan, V. K.; Lauhon, L. J.; Hersam, M. C. Suppressing Ambient Degradation of Exfoliated InSe Nanosheet Devices via Seeded Atomic Layer Deposition Encapsulation. *Nano Lett.* **2018**, *18*, 7876–7882.
- (21) Ho, P.-H.; Chang, Y.-R.; Chu, Y.-C.; Li, M.-K.; Tsai, C.-A.; Wang, W.-H.; Ho, C.-H.; Chen, C.-W.; Chiu, P.-W. High-Mobility InSe Transistors: The Role of Surface Oxides. *ACS Nano* **2017**, *11*, 7362–7370.
- (22) Liang, G.; Wang, Y.; Han, L.; Yang, Z.-X.; Xin, Q.; Kudrynskiy, Z. R.; Kovalyuk, Z. D.; Patané, A.; Song, A. Improved performance of InSe field-effect transistors by channel encapsulation. *Semicond. Sci. Technol.* **2018**, *33*, 06LT01.
- (23) Li, Q.; Zhou, Q.; Shi, L.; Chen, Q.; Wang, J. Recent advances in oxidation and degradation mechanisms of ultrathin 2D materials under ambient conditions and their passivation strategies. *J. Mater. Chem. A* **2019**, *7*, 4291–4312.
- (24) Li, Q.; Shi, L.; Wu, R.; Lin, C.; Bai, X.; Ouyang, Y.; Baraiya, B. A.; Jha, P. K.; Wang, J. Unveiling chemical reactivity and oxidation of 1T-phased group VI disulfides. *Phys. Chem. Chem. Phys.* **2019**, *21*, 17010–17017.
- (25) Liu, H.; Han, N.; Zhao, J. Atomistic insight into the oxidation of monolayer transition metal dichalcogenides: from structures to electronic properties. *RSC Adv.* **2015**, *5*, 17572–17581.
- (26) Geim, A. K.; Grigorieva, I. V. Van der Waals heterostructures. *Nature* **2013**, *499*, 419–425.
- (27) Galbiati, M.; Zatko, V.; Godel, F.; Hirschauer, P.; Vecchiola, A.; Bouzehouane, K.; Collin, S.; Servet, B.; Cantarero, A.; Petroff, F.; Martin, M.-B.; Dlubak, B.; Seneor, P. Very Long Term Stabilization of a 2D Magnet down to the Monolayer for Device Integration. *ACS Appl. Electron. Mater.* **2020**, *2*, 3508–3514.
- (28) Zhu, X.; Zhang, T.; Jiang, D.; Duan, H.; Sun, Z.; Zhang, M.; Jin, H.; Guan, R.; Liu, Y.; Chen, M. Stabilizing black phosphorus nanosheets via edge-selective bonding of sacrificial C<sub>60</sub> molecules. *Nat. Commun.* **2018**, *9*, 4177.
- (29) Shi, F.; Dong, X.; Huang, K.; Geng, Z.; Wang, X.; Yang, X.; Wang, C.; Zhang, W.; Feng, S. Stabilizing black phosphorus via inorganic small-molecular H<sub>3</sub>BO<sub>3</sub>. *Chem. Commun.* **2020**, *56*, 11418–11421.
- (30) Pető, J.; Ollár, T.; Vancsó, P.; Popov, Z. I.; Magda, G. Z.; Dobrik, G.; Hwang, C.; Sorokin, P. B.; Tapasztó, L. Spontaneous doping of the basal plane of MoS<sub>2</sub> single layers through oxygen



substitution under ambient conditions. *Nat. Chem.* **2018**, *10*, 1246–1251.

(31) Zhou, Q.; Chen, Q.; Tong, Y.; Wang, J. Light-Induced Ambient Degradation of Few-Layer Black Phosphorus: Mechanism and Protection. *Angew. Chem., Int. Ed.* **2016**, *55*, 11437–11441.

(32) Yang, B.; Wan, B.; Zhou, Q.; Wang, Y.; Hu, W.; Lv, W.; Chen, Q.; Zeng, Z.; Wen, F.; Xiang, J.; Yuan, S.; Wang, J.; Zhang, B.; Wang, W.; Zhang, J.; Xu, B.; Zhao, Z.; Tian, Y.; Liu, Z. Te-Doped Black Phosphorus Field-Effect Transistors. *Adv. Mater.* **2016**, *28*, 9408–9415.

(33) Favron, A.; Gaufres, E.; Fossard, F.; Phaneuf-L'Heureux, A.-L.; Tang, N. Y.-W.; Lévesque, P. L.; Loiseau, A.; Leonelli, R.; Francoeur, S.; Martel, R. Photooxidation and quantum confinement effects in exfoliated black phosphorus. *Nat. Mater.* **2015**, *14*, 826–832.

(34) Su, C.; Yin, Z.; Yan, Q.-B.; Wang, Z.; Lin, H.; Sun, L.; Xu, W.; Yamada, T.; Ji, X.; Zettsu, N.; Teshima, K.; Warner, J. H.; Dincă, M.; Hu, J.; Dong, M.; Su, G.; Kong, J.; Li, J. Waterproof molecular monolayers stabilize 2D materials. *Proc. Natl. Acad. Sci. U.S.A.* **2019**, *116*, 20844–20849.

(35) Taube, H. Rates and Mechanisms of Substitution in Inorganic Complexes in Solution. *Chem. Rev.* **1952**, *50*, 69–126.

(36) Mønsted, L.; Mønsted, O. Mechanism of thermal and photochemical ligand substitution reactions of chromium(III) and other octahedral metal complexes. *Coord. Chem. Rev.* **1989**, *94*, 109–150.

(37) Gish, J. T.; Lebedev, D.; Stanev, T. K.; Jiang, S.; Georgopoulos, L.; Song, T. W.; Lim, G.; Garvey, E. S.; Valdman, L.; Balogun, O.; Sofer, Z.; Sangwan, V. K.; Stern, N. P.; Hersam, M. C. Ambient-Stable Two-Dimensional CrI<sub>3</sub> via Organic-Inorganic Encapsulation. *ACS Nano* **2021**, *15*, 10659–10667.

(38) Nicolosi, V.; Chhowalla, M.; Kanatzidis, M. G.; Strano, M. S.; Coleman, J. N. Liquid Exfoliation of Layered Materials. *Science* **2013**, *340*, 1226419.

(39) Li, J.; Song, P.; Zhao, J.; Vaklinova, K.; Zhao, X.; Li, Z.; Qiu, Z.; Wang, Z.; Lin, L.; Zhao, M.; Herng, T. S.; Zuo, Y.; Jonhson, W.; Yu, W.; Hai, X.; Lyu, P.; Xu, H.; Yang, H.; Chen, C.; Pennycook, S. J.; Ding, J.; Teng, J.; Castro Neto, A. H.; Novoselov, K. S.; Lu, J. Printable two-dimensional superconducting monolayers. *Nat. Mater.* **2021**, *20*, 181–187.

(40) Ryder, C. R.; Wood, J. D.; Wells, S. A.; Yang, Y.; Jariwala, D.; Marks, T. J.; Schatz, G. C.; Hersam, M. C. Covalent functionalization and passivation of exfoliated black phosphorus via aryl diazonium chemistry. *Nat. Chem.* **2016**, *8*, 597–602.

(41) Hanlon, D.; Backes, C.; Doherty, E.; Cucinotta, C. S.; Berner, N. C.; Boland, C.; Lee, K.; Harvey, A.; Lynch, P.; Gholamvand, Z. Liquid exfoliation of solvent-stabilized few-layer black phosphorus for applications beyond electronics. *Nat. Commun.* **2015**, *6*, 8563.

(42) Abellán, G.; Wild, S.; Lloret, V.; Scheuschner, N.; Gillen, R.; Mundloch, U.; Maultzsch, J.; Varela, M.; Hauke, F.; Hirsch, A. Fundamental insights into the degradation and stabilization of thin layer black phosphorus. *J. Am. Chem. Soc.* **2017**, *139*, 10432–10440.

(43) Backes, C.; Berner, N. C.; Chen, X.; Lafargue, P.; LaPlace, P.; Freeley, M.; Duesberg, G. S.; Coleman, J. N.; McDonald, A. R. Functionalization of liquid-exfoliated two-dimensional 2H-MoS<sub>2</sub>. *Angew. Chem., Int. Ed.* **2015**, *54*, 2638–2642.

(44) Abellán, G.; Lloret, V.; Mundloch, U.; Marcia, M.; Neiss, C.; Görling, A.; Varela, M.; Hauke, F.; Hirsch, A. Noncovalent functionalization of black phosphorus. *Angew. Chem., Int. Ed.* **2016**, *55*, 14557–14562.

(45) Guo, Z.; Chen, S.; Wang, Z.; Yang, Z.; Liu, F.; Xu, Y.; Wang, J.; Yi, Y.; Zhang, H.; Liao, L.; Chu, P. K.; Yu, X.-F. Metal-Ion-Modified Black Phosphorus with Enhanced Stability and Transistor Performance. *Adv. Mater.* **2017**, *29*, 1703811.

(46) Shi, L.; Zhou, Q.; Zhao, Y.; Ouyang, Y.; Ling, C.; Li, Q.; Wang, J. Oxidation mechanism and protection strategy of ultrathin Indium Selenide: Insight from Theory. *J. Phys. Chem. Lett.* **2017**, *8*, 4368–4373.

(47) Zhang, T.; Wan, Y.; Xie, H.; Mu, Y.; Du, P.; Wang, D.; Wu, X.; Ji, H.; Wan, L. Degradation chemistry and stabilization of exfoliated

few-layer black phosphorus in water. *J. Am. Chem. Soc.* **2018**, *140*, 7561–7567.

(48) Scharf, U.; Schneider, H.; Baiker, A.; Wokaun, A. Chromia Supported on Titania .III. Structure and Spectroscopic Properties. *J. Catal.* **1994**, *145*, 464–478.

(49) Long, D. A. Infrared and Raman characteristic group frequencies. Tables and charts George Socrates, Third Edition; John Wiley and Sons, Ltd.: Chichester, 2001. *J. Raman Spectrosc.* **2004**, *35*, 905.

(50) Xiang, K.-h.; Pandey, R.; Recio, J. M.; Francisco, E.; Newsam, J. M. A Theoretical Study of the Cluster Vibrations in Cr<sub>2</sub>O<sub>2</sub>, Cr<sub>2</sub>O<sub>3</sub>, and Cr<sub>2</sub>O<sub>4</sub>. *J. Phys. Chem. A* **2000**, *104*, 990–994.

(51) Arévalo-López, A. n. M.; Alario-Franco, M. A. Reliable method for determining the oxidation state in chromium oxides. *Inorg. Chem.* **2009**, *48*, 11843–11846.

(52) Kytöki, A.; Jacobs, J.-P.; Hakuli, A.; Meriläinen, J.; Brongersma, H. H. Surface Characteristics and Activity of Chromia/Alumina Catalysts Prepared by Atomic Layer Epitaxy. *J. Catal.* **1996**, *162*, 190–197.

(53) Soler, J. M.; Artacho, E.; Gale, J. D.; García, A.; Junquera, J.; Ordejón, P.; Sánchez-Portal, D. The SIESTA method for ab initio order-N materials simulation. *J. Phys.: Condens. Matter* **2002**, *14*, 2745–2779.

(54) Abellán, G.; Wild, S.; Lloret, V.; Scheuschner, N.; Gillen, R.; Mundloch, U.; Maultzsch, J.; Varela, M.; Hauke, F.; Hirsch, A. Fundamental Insights into the Degradation and Stabilization of Thin Layer Black Phosphorus. *J. Am. Chem. Soc.* **2017**, *139*, 10432–10440.

(55) Huang, B.; Cenker, J.; Zhang, X.; Ray, E. L.; Song, T.; Taniguchi, T.; Watanabe, K.; McGuire, M. A.; Xiao, D.; Xu, X. Tuning inelastic light scattering via symmetry control in the two-dimensional magnet CrI<sub>3</sub>. *Nat. Nanotechnol.* **2020**, *15*, 212–216.

(56) Webster, L.; Liang, L.; Yan, J.-A. Distinct spin–lattice and spin–phonon interactions in monolayer magnetic CrI<sub>3</sub>. *Phys. Chem. Chem. Phys.* **2018**, *20*, 23546–23555.

(57) Acharya, S.; Pashov, D.; Rudenko, A.; Rösner, M.; Schilfgaarde, M.; Katsnelson, M. Excitons in Bulk and Layered Chromium Trihalides: From Frenkel to the Wannier-Mott Limit. 2021, arXiv. <https://arxiv.org/abs/2110.08174v1>.

(58) Palik, E. D.; Furdyna, J. K. Infrared and microwave magnetoplasma effects in semiconductors. *Rep. Prog. Phys.* **1970**, *33*, 1193–1322.

(59) Zhong, D.; Seyler, K. L.; Linpeng, X.; Cheng, R.; Sivadas, N.; Huang, B.; Schmidgall, E.; Taniguchi, T.; Watanabe, K.; McGuire, M. A.; Yao, W.; Xiao, D.; Fu, K.-C.; Xu, X. Van der Waals engineering of ferromagnetic semiconductor heterostructures for spin and valleytronics. *Sci. Adv.* **2017**, *3*, No. e1603113.

(60) Thiel, L.; Wang, Z.; Tschudin, M. A.; Rohner, D.; Gutiérrez-Lezama, I.; Ubrig, N.; Gibertini, M.; Giannini, E.; Morpurgo, A. F.; Maletinsky, P. Probing magnetism in 2D materials at the nanoscale with single-spin microscopy. *Science* **2019**, *364*, 973–976.